processes

MDPI

Article

Mechanism of Casing Deformation of Shale Gas Platform Wells in Luzhou Block Before Fracturing and Countermeasures for Prevention and Control

Xiaojun Zhang [1], Jun Li [1,2,*], Yuxuan Zhao [3], Wei Cao [4], Wenbo Zhang [3], Zongyu Lu [3] and Gonghui Liu [5]

[1] School of Petroleum Engineering, China University of Petroleum (Beijing), Changping, Beijing 102249, China; xiaojun970216@163.com
[2] School of Petroleum, China University of Petroleum (Beijing) Karamay Campus, Karamay 834000, China
[3] Engineering Technology Research Institute, Xinjiang Oilfield Company, Karamay 834000, China; zhao920810@126.com (Y.Z.); zxj805paper@163.com (W.Z.); luzy446@163.com (Z.L.)
[4] Sichuan Jewel Flower Xinsheng Oil & Gas Operation Service Co., Chengdu 610051, China; cuppaper806@163.com
[5] Institute of Oil and Gas Research, Beijing University of Technology, Chaoyang, Beijing 100021, China; lijun_paper8@126.com
* Correspondence: lijun_paper806@163.com

Abstract: The deep shale gas resources in the Luzhou area of the southern Sichuan Basin are abundant and have been identified as a key replacement field for natural gas development following the medium-to-shallow shale gas fields in Changning and Weiyuan. However, the frequent occurrence of "pre-deformation without fracturing" in horizontal wells has significantly restricted large-scale production. In this study, the Lu203 and Yang101 well areas were analyzed to investigate the characteristics of casing deformation and the correlation with faults and natural fractures (fracture systems). A numerical model of multi-stage fracturing for platform wells was established based on microseismic event data, and the effects of fracturing on the stress and casing stress of adjacent wells were simulated and analyzed. The results indicate that the development of fracture systems is the primary cause of the "pre-deformation without fracturing" phenomenon. The propagation of fracturing fluid through fractures significantly increases the stress and loading around adjacent wells, causing casing stress to exceed its yield strength. To mitigate this issue, a method involving the injection of approximately 10 MPa of internal casing pressure into unfractured wells was proposed, effectively reducing the risk of casing deformation and failure. This provides technical support for the efficient development of deep shale gas.

Keywords: shale gas well; deformation before fracturing; finite element model; casing deformation prevention and control

check for updates

Academic Editors: Chuanliang Yan and Dicho Stratiev

Received: 15 November 2024
Revised: 18 January 2025
Accepted: 4 February 2025
Published: 10 February 2025

Citation: Zhang, X.; Li, J.; Zhao, Y.; Cao, W.; Zhang, W.; Lu, Z.; Liu, G. Mechanism of Casing Deformation of Shale Gas Platform Wells in Luzhou Block Before Fracturing and Countermeasures for Prevention and Control. *Processes* **2025**, *13*, 479. https://doi.org/10.3390/pr13020479

Copyright: © 2025 by the authors. Licensee MDPI, Basel, Switzerland. This article is an open access article distributed under the terms and conditions of the Creative Commons Attribution (CC BY) license (https://creativecommons.org/licenses/by/4.0/).

1. Introduction

The deep shale gas reserves in the Luzhou block of the southern Sichuan Basin have been identified as an important exploration area for China's future natural gas resources [1]. The combination of platform horizontal wells and multi-stage fracturing technology has been recognized as a key approach for its efficient development [2,3]. However, during the development process, casing deformation problems have been widely observed and have become a major challenge restricting the efficient exploitation of shale gas. According to statistics, by the end of 2023, a total of 103 deep shale gas wells in the southern Sichuan Basin, Luzhou block, had experienced casing deformation [4], with the casing deformation

rate in the Luzhou 203 well area reaching as high as 68.6% [5]. In addition, severe "pre-deformation without fracturing" has been reported in this area, meaning that casing deformation occurs prior to fracturing operations, further compromising the effectiveness of fracturing treatments. These challenges highlight the need for further investigation into the mechanisms underlying casing deformation and the development of effective mitigation strategies to support the large-scale development of deep shale gas resources in the Luzhou block.

Extensive research has been conducted by scholars both domestically and internationally to address the problem of casing deformation in shale gas wells. It is generally recognized that fault activation and subsequent shear slip induced by fracturing are among the primary causes of casing deformation. Lu et al. [6] indicated that fault slip shear is the primary cause of casing deformation, characterized by a "dense at the heel and sparse at the toe" pattern, with casing deformation due to fault slip shear accounting for 75% of the total deformation points. It was proposed by Zoback et al. [7] that large-scale fracturing operations lead to alterations in the original in situ stress field, resulting in slippage along discontinuities such as faults and natural fractures of various scales. This stress redistribution subsequently induces block movements in the formation, causing shear deformation and failure of the casing. Chipperfield et al. [8] highlighted that the significant scale of hydraulic fracturing, including a high number of fracture stages, large injection volumes, and complex fracture network formation, contributes to changes in the stress field. These changes ultimately lead to the slip of natural fractures and faults, resulting in casing deformation. Dong et al. [9], using the Mohr–Coulomb criterion, analyzed the conditions for the shear slip of natural fractures and faults and investigated fault stability. Their findings indicated that most natural fractures and faults are likely to be activated under high fracturing pressure. Chen et al. [10,11], based on field engineering data, summarized three primary pathways through which fracturing fluid enters faults: artificial hydraulic fractures, axial fractures along the wellbore, and micro-annuli formed in the cement sheath due to repeated fracturing. They utilized a seismic source mechanism analysis and deformation data to calculate fault slip radii and displacement. Yin [12,13] and Xu [14] argued that large-scale fracturing allows fluids to penetrate faults, increasing pore pressure within the fault and reducing the effective normal stress on the fault plane, which, in turn, triggers fault activation and slip, eventually causing shear deformation of the casing. Furthermore, Zhao et al. [15], integrating the characteristics of casing deformation in shale gas wells in the Sichuan Basin with geological data, performed a comprehensive analysis based on seismic interpretation (faults or major fracture zones), logging interpretation (anisotropy of near-well formations), and interlayer penetration. They concluded that casing deformation tends to occur in well segments characterized by significant geological heterogeneity, developed natural fractures, or fault presence. Based on this, they established a fault slip prediction model under hydraulic fracturing conditions. Zhao et al. [16] proposed a method for characterizing the casing deformation caused by fault slips at a real scale. The research results indicate that the casing deformation process due to fault slip shear can be divided into three stages: the triggering and activation stage, the accelerated sliding stage, and the decelerated sliding stage. Although numerous scholars have systematically elaborated on the fracture slip mechanism of casing deformation, the deformation mechanism of the pre-deformation phenomenon in platform wells in the Luzhou area remains unclear. Therefore, there is an urgent need to conduct research on the mechanism of pre-deformation in platform wells.

Based on the mechanisms of shear deformation in casings caused by natural fractures and fault slips, a series of measures to reduce the risk of casing deformation have been proposed by scholars, both domestically and internationally, through numerical simulations and laboratory experiments. These measures can be categorized into two main approaches.

The first approach focuses on the properties of the casing itself and the cementing process, aiming to reduce the deformation risks by enhancing the shear strength of the casing or alleviating the stress exerted on it. For example, Liu et al. [17] suggested incorporating hollow glass microspheres into cement slurry to mitigate the impact of fault slips on the casing. The hollow microspheres, once crushed during shearing in the cement sheath, create compressive space to absorb the formation displacement, thereby reducing the casing shear deformation. Zhao et al. [18] recommended a method for optimizing the casing selection in shear deformation zones by increasing the casing wall thickness and upgrading the steel grades, which helps alleviate deformation under smaller displacement conditions. The second approach focuses on reducing the risk of natural fractures and fault slips by controlling the fluid pressure increments to minimize the likelihood of fractures or fault activation. For instance, Tong et al. [19] and Zhang et al. [20] proposed using fracture temporary plugging techniques to inhibit the propagation of fracturing fluid in faults or natural fractures, thereby reducing the risk of slip activation. Chen et al. [21] suggested controlling the fault activation length and the number of activated natural fractures by reducing the fracturing fluid injection rate and total injection volume, which decreases the probability of casing deformation. Lu et al. [22] emphasized that fault slip risks are significantly influenced by factors such as the interface friction coefficient and fluid pressure. By reducing the fluid pressure, the probability of fault slips can be effectively lowered. Han et al. [5] proposed mitigating casing deformation caused by geological factors by avoiding high-risk fault zones and selecting well locations in areas with low stress mechanism factors. Lei et al. [23,24] proposed the addition of an annular buffer layer in the wellbore to reduce the casing shear deformation and validated through finite element methods that the buffer layer can effectively reduce casing deformation. These measures have been tested in the field in blocks such as the Changning and Weiyuan blocks in the Sichuan Basin, yielding certain positive results. However, for the pre-deformation phenomenon in platform wells in the Luzhou block, effective prevention and control measures have not yet been developed, which severely impacts the development process.

Compared to medium-deep shale gas blocks (e.g., the Changning block), the Luzhou block, particularly its deep reservoirs represented by the Lu203 well area, exhibits more developed fractures, higher formation pressures, and more severe casing deformation, with deformation occurring at higher grades. These issues have significantly impacted the wellbore integrity and development performance, particularly with the frequent occurrence of “pre-deformation without fracturing” wells. However, the deformation mechanisms underlying this phenomenon remain insufficiently studied, and effective prevention and control measures are lacking. In this study, the controlling factors and mechanisms of casing deformation in unfractured wells on platforms were systematically investigated, and targeted prevention and control strategies were proposed. First, based on actual data from the Luzhou block, the deformation phenomena and characteristics of “pre-deformation without fracturing” wells were statistically analyzed, revealing a strong correlation between casing deformation and the development of natural fractures and faults. Second, a numerical model for the multi-stage fracturing of platform wells was established to systematically analyze the changes in geo-stress and casing stress around unfractured wells during fracturing operations. The key mechanisms of casing deformation in unfractured wells on platforms were elucidated. Finally, innovative measures, such as pre-pressurization of the casing, were proposed to prevent and control the casing deformation in unfractured wells. These strategies provide important theoretical foundations and practical guidance for the efficient development of deep shale gas. This research not only deepens the understanding of casing deformation phenomena in unfractured wells on platforms but also offers valuable solutions for addressing similar challenges in other shale gas blocks.

2. Casing Deformation Characteristics in the Luzhou Block

2.1. Overview of Casing Deformation

The Luzhou block primarily consists of two production areas: Lu203 and Yang101. According to statistical data, 43 wells with casing deformation have been identified in the Luzhou block. Among these, 36 wells are located in the Lu203 area, and 7 wells are in the Yang101 area. In the Lu203 area, 28 wells experienced pre-deformation before fracturing, accounting for 77.78% of the deformed wells. In contrast, 28.57% of the deformed wells in the Yang101 area showed pre-deformation. These results are shown in Figure 1.

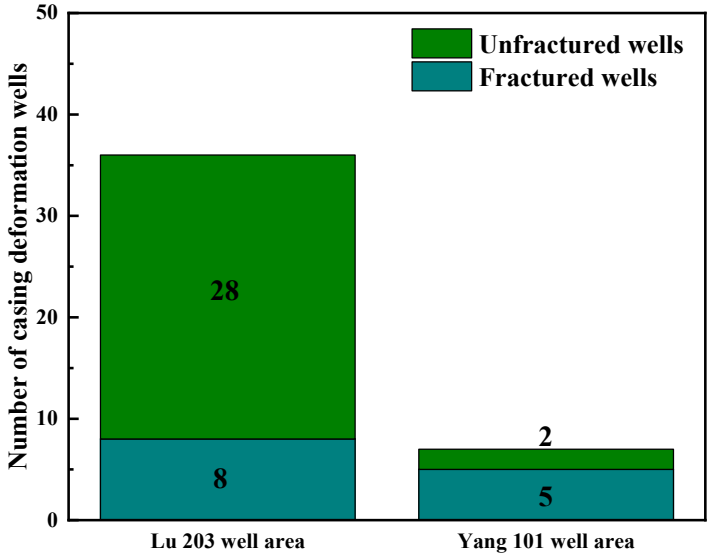

Figure 1. Statistical results of casing deformation wells in the Luzhou block.

Based on the casings' inner diameter, casing deformation in the Luzhou block is classified into three levels: A, B, and C. Level A refers to casing with an inner diameter greater than 85 mm. Level B includes casing with an inner diameter of 54–85 mm. Level C applies to casing with an inner diameter of less than 54 mm. For Level A and B deformations, small bridge plugs or combined fracturing techniques are typically employed to improve the well conditions. However, for Level C deformations, due to the severe damage, fracturing operations are currently suspended. A further statistical analysis of the deformation levels in the Luzhou block indicates that Level A deformation is predominant in the Lu203 area, accounting for 46% of the deformed wells, while Levels B and C each account for 26%. In the Yang101 area, Level A and B deformations are the most common, representing 50% and 39%, respectively, with Level C deformation accounting for only 11%. Overall, the Luzhou block exhibits a high occurrence of casing deformation, with pre-deformation before fracturing being particularly prominent. The severity of casing deformation has resulted in some wells temporarily losing production capacity, significantly restricting the overall production and development efficiency of the block.

2.2. Distribution Characteristics of Casing Deformation Points

A large number of microseismic monitoring results indicate that during multi-stage hydraulic fracturing of platform multi-branch wells, hydraulic fractures are prone to connecting with nearby fracture systems. This often results in severe casing deformation near the fracture zones. The deformation points are typically located at considerable distances from the target fracturing segments. Based on the ant-tracking fracture interpretation, the correlation between casing deformation points and complex geological features, such as natural fractures and abnormal formation curvature, was analyzed. A statistical analysis was conducted to examine the relationship between casing deformation points, the distance

to natural fractures, and the angle of natural fractures (i.e., the angle between the natural fracture strike and the horizontal wellbore). The results are shown in Figure 2. It was observed that 53% of the casing deformation points are located within fracture zones or within 100 m of fracture zones. Additionally, 62% of deformation points are concentrated in areas where the natural fracture angle ranges from 16° to 45°. These findings demonstrate a strong correlation between casing deformation and natural fractures.

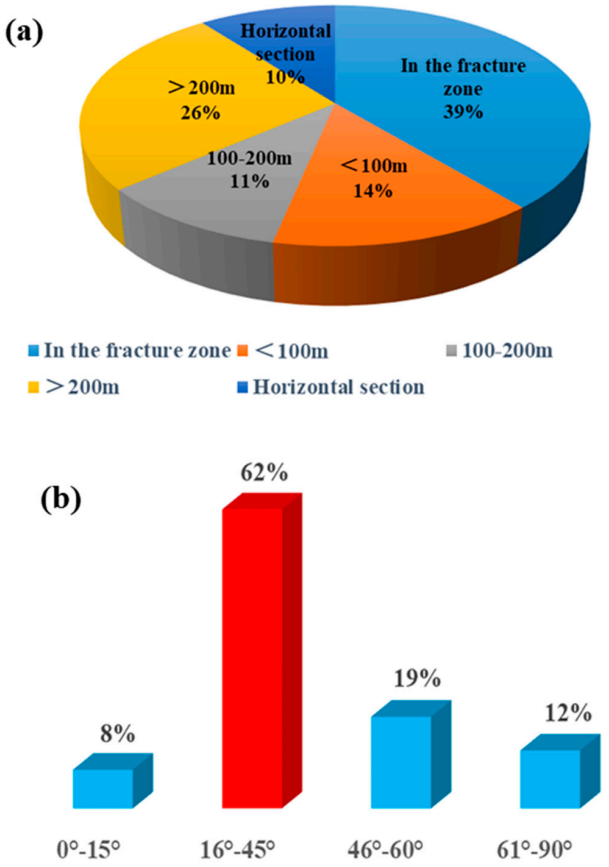

Figure 2. The correlation between casing deformation points and natural fractures in the Luzhou block. (**a**) Relationship between casing deformation points and natural fracture distances. (**b**) Relationship between casing deformation points and natural fracture angles.

Based on the fracture prediction and evaluation results for the H1–H4 platforms in the Lu203 area, as shown in Figure 3, a nearly north–south-oriented fault is developed between the H1 and H2 platforms. The fracture zones around this fault are significantly influenced by its orientation, and the natural fracture zones intersect the horizontal wellbores at certain angles. A total of 16 fracturing wells were designed for the H1–H4 platforms, of which 11 wells experienced casing deformation. Among them, seven wells were unfractured, and the proportion of pre-deformation before fracturing reached 68.75%. Among the 16 casing deformation points, 10 are located within natural fracture zones or regions of abnormal formation curvature, accounting for 62.5%. These findings further indicate a strong correlation between the pre-deformation phenomenon and casing deformation locations with natural fracture zones and regions of abnormal formation curvature. In summary, casing deformation in the Lu203 area is primarily distributed in regions associated with natural fractures and fault activity. Moreover, casing deformation often does not occur during fracturing operations in the same well. This suggests that the development of natural fractures and faults is a key factor contributing to the high number of pre-deformation wells in this area.

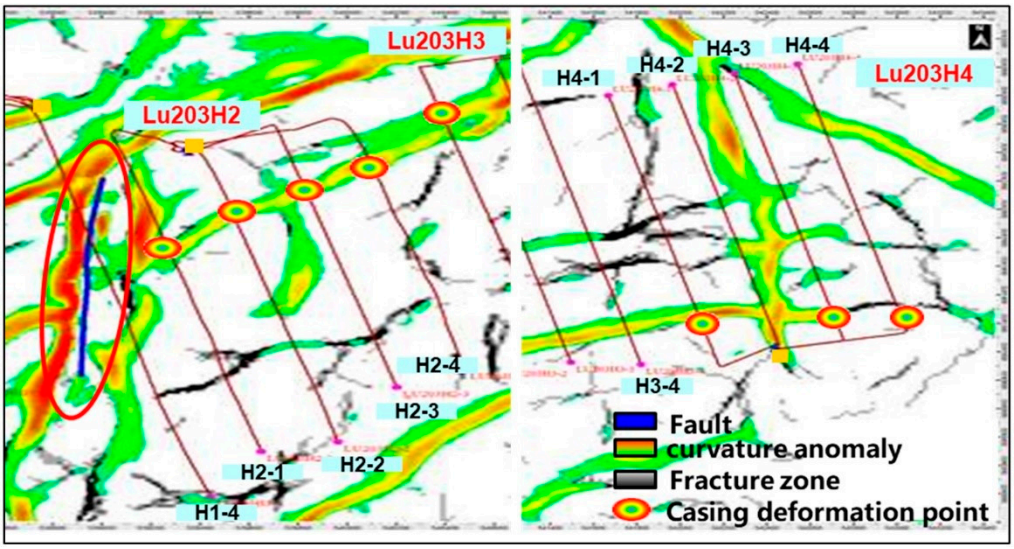

Figure 3. Relationship between fracture distribution and casing deformation point of platforms H1–H4 in the Lu203 well area.

2.3. Analysis of the Causes of Deformation Before Fracturing

Based on the above analysis, the casing deformation points of platform unfractured wells show a strong correlation with natural fractures, fault development zones, and regions of abnormal formation curvature. Figure 4 illustrates the possible causes of pre-deformation in platform wells. In the figure, ① represents artificial hydraulic fractures, ② represents the connection between artificial hydraulic fractures and the fracture system (faults or natural fractures), ③ represents the diffusion of fracturing fluid along fracture zones under pressure gradients, and ④ represents casing deformation in platform unfractured wells.

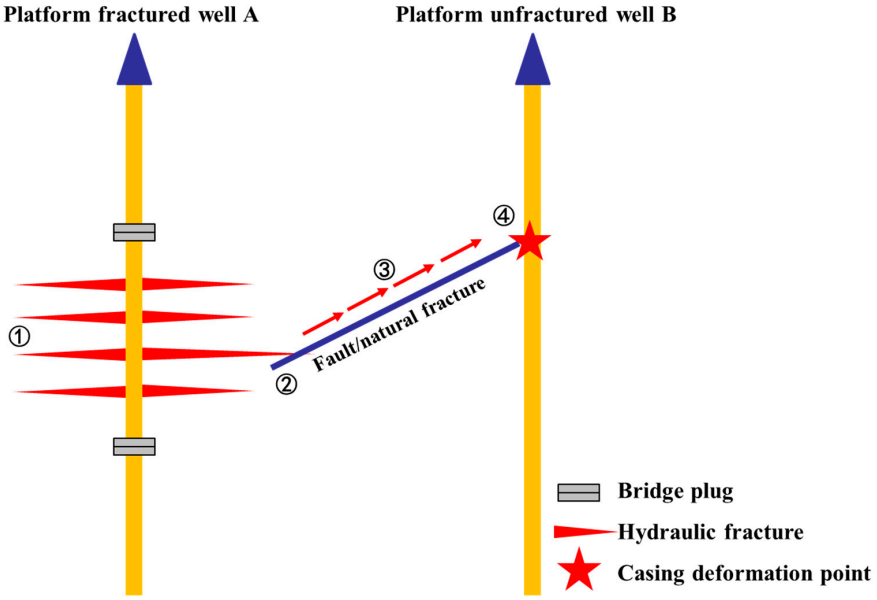

Figure 4. Schematic of casing deformation before fracturing in platform wells.

The causes of casing deformation in platform unfractured wells are preliminarily attributed to two main factors. First, under the original geological state, fractures remain relatively stable as the frictional force on the fracture surface exceeds the shear stress. When hydraulic fractures connect with the fracture system, fracturing fluid continuously enters the fracture surface, causing the pore pressure to increase and gradually reducing the frictional force. Once the frictional force equals the shear stress, the fracture reaches a

critical sliding state. A further injection of fracturing fluid activates the fracture, resulting in a sliding motion. This process exerts force on the casing of the unfractured well, leading to casing deformation. The mechanism of casing deformation caused by fault activation and sliding has been extensively studied. Second, when fracturing fluid enters the fracture system without activating the fractures, it diffuses along the fracture orientation, causing stress concentration in localized regions around the platform unfractured wells. This stress concentration subjects the casing to high localized loads, increasing the risk of deformation. This study focuses on analyzing the mechanism of casing deformation in platform unfractured wells caused by localized loads.

3. Research Method

3.1. Characterization of Microseismic Event Point Distribution

Microseismic monitoring is conducted based on the principle of acoustic emission, where geophones installed in neighboring wells are used to capture micro-seismic wave signals generated during rock failure in the fracturing process. These signals are utilized to describe the evolution process and spatial distribution of fractures, enabling the accurate inference of fracture geometry. Furthermore, the stimulated reservoir volume and its distribution characteristics are evaluated based on this analysis.

Figure 5 illustrates the comprehensive microseismic event map for the first ten stages of fracturing in Well X-6 of the Lu203 well area. In the figure, circles of different colors represent microseismic events corresponding to individual fracturing stages. It can be observed that, after the first ten stages of fracturing, microseismic events are widely distributed within the stimulated region around the wellbore, indicating the formation of a complex fracture network in the reservoir. Additionally, the microseismic events exhibit a clearly uneven spatial distribution around the wellbore. Events from certain fracturing stages are observed near the neighboring wells X-4 and X-5. After Stage 8 fracturing, a small number of microseismic events are detected near adjacent wells, while the natural fracture zone shows a strong response following Stage 9 fracturing. The black arrows in the figure indicate the orientation of natural fractures, with microseismic events extending along and intersecting the fractures and the wellbore. A significant number of events are distributed on both sides of Well X-5 and to the east of Well X-4. Influenced by natural fractures, some microseismic events recorded after Stage 10 fracturing overlap with those from Stage 9. Along the natural fracture zone, microseismic events of various colors are observed, suggesting that the area underwent multiple fracturing stimulations, with some regions being re-stimulated two or more times.

According to well history records, the entire wellbore of Well X-6 has undergone fracturing operations, whereas Wells X-4 and X-5 have yet to begin fracturing. During the bridge plug pumping operation in Well X-5, obstruction was encountered at a depth of 4593 m, preventing the bridge plug from descending. A preliminary analysis suggests that the obstruction was caused by casing deformation. As shown in Figure 5, the location of the obstruction coincides with the distribution zone of natural fractures. To address this, a simplified processing of the microseismic event point distribution for the relevant fracturing stages (Stages 6 to 10) associated with the obstruction location was performed. Specifically, isolated event points and those distant from the casing deformation failure site were excluded, and the microseismic event points for each fracturing stage were delineated using regular geometric boundaries. This approach allowed for the characterization of the stimulation range and distribution features for different fracturing stages. As illustrated in Figure 6, the color gradient indicates the intensity of the microseismic signals. It can also be observed that certain localized areas around the wellbore exhibit overlapping "fracture clusters" from different fracturing stages, indicating that these regions have been subjected

to repeated fracturing, often more than twice. Consequently, the rocks in these areas have undergone multiple disruptions, leading to varying degrees of degradation in their rock properties. Accordingly, parameters such as the elastic modulus are expected to experience different changes.

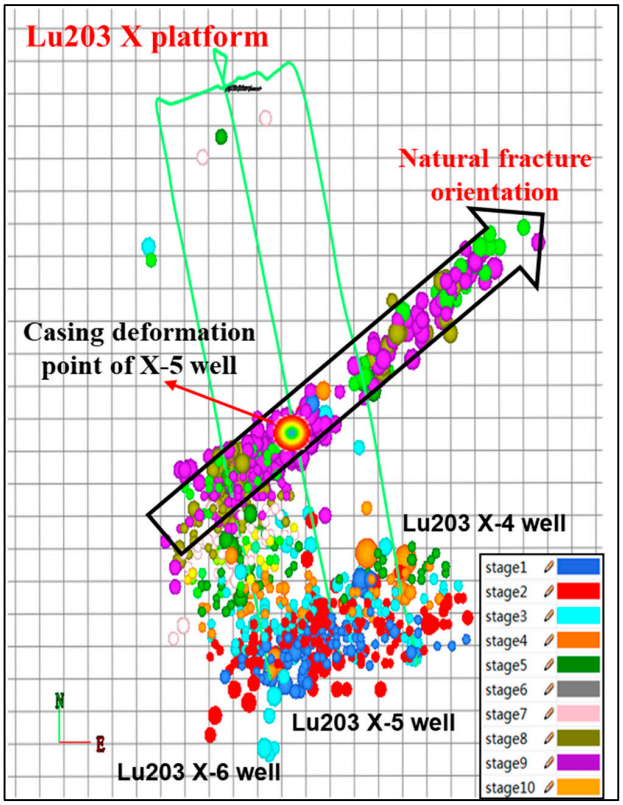

Figure 5. Distribution characteristics of microseismic signals from 1 to 10 fracturing of Well X-6 in the Lu203 well area.

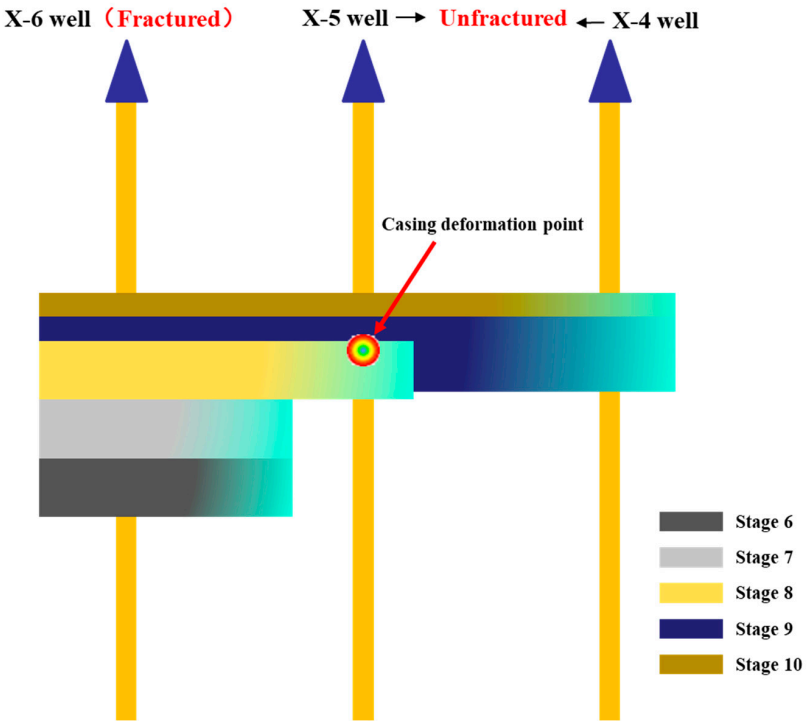

Figure 6. Simplified processing map of microseismic event points for the X Platform.

3.2. Dynamic Geo-Stress Variation Model for Multi-Stage Fracturing

3.2.1. Pore Pressure-Induced Geo-Stress Variation Model

During the fracturing process of shale gas horizontal wells, the injection of high-pressure fracturing fluid induces an increase in the formation pore pressure, which subsequently causes variations in in situ stresses. According to Hooke's Law and the pore-elastic theory [25,26], the relationship between formation pore pressure and geo-stress can be expressed by Equation (1).

$$\sigma_{ij} = \frac{E}{1+\nu}\left[\frac{\nu}{1-2\nu}\varepsilon_{kk}\delta_{ij} + \varepsilon_{ij}\right] + \alpha p\delta_{ij} \tag{1}$$

By differentiating Equation (1), the expression for the induced stress field resulting from the pore pressure variations can be derived, as shown in Equation (2).

$$\begin{bmatrix} \Delta\sigma_{xx} \\ \Delta\sigma_{yy} \\ \Delta\sigma_{zz} \end{bmatrix} = \frac{E}{(1+\nu)(1-2\nu)}\begin{bmatrix} 1-\nu & \nu & \nu \\ \nu & 1-\nu & \nu \\ \nu & \nu & 1-\nu \end{bmatrix} \times \begin{bmatrix} \Delta\varepsilon_x \\ \Delta\varepsilon_y \\ \Delta\varepsilon_z \end{bmatrix} + \alpha\Delta p \begin{bmatrix} 1 \\ 1 \\ 1 \end{bmatrix} \tag{2}$$

Here, σ_{ij} and ε_{ij} represent the stress and strain tensors, respectively; $\Delta\sigma_{ij}$ denotes the induced stress; $\Delta\varepsilon_{ij}$ represents the Kronecker delta; p and Δp correspond to the pore fluid pressure and its variation, respectively; and E and ν represent the elastic modulus and Poisson's ratio of the formation, respectively.

The increase in pore pressure during hydraulic fracturing induces a certain degree of deformation in the formation. When calculating the stress field in the formation during fracturing, the coupling between rock deformation and formation fluid flow must be resolved. These two processes interact through changes in parameters such as porosity, permeability, and saturation caused by rock deformation. The governing equation for fracturing fluid flow and the fluid seepage equation in shale reservoirs are expressed as Equations (3) and (4), respectively.

$$\frac{\partial}{\partial t}(\nabla S_w\rho_w\phi) + \nabla(\rho_w v_w) + q_w = 0 \tag{3}$$

$$v_w = -\frac{kk_w}{\mu_w}(\nabla p + \rho_w g\nabla H) \tag{4}$$

The deformation of the formation induces changes in its permeability, as expressed in Equation (5).

$$k = k_0\frac{(1+\frac{\varepsilon_v}{\phi})^3}{(1+\varepsilon_v)} \tag{5}$$

Here, ρ_w represents the density of the liquid phase; v_w denotes the velocity of the liquid phase; q_w corresponds to the source or sink term of the liquid phase; k_0 and k_w represent the initial permeability of the formation and the relative permeability of the water phase, respectively; μ_w denotes the liquid phase viscosity; H represents the reservoir burial depth; ϕ denotes the porosity; and ε_v represents the volumetric strain of the rock.

3.2.2. Mathematical Model of Seepage–Stress Coupling

The effective stress is commonly used to calculate seepage–stress coupling.

(1) Principle of Effective Stress

Based on the principle of effective stress [27–29], the total stress is composed of the effective stress, pore water pressure, and pore gas pressure, as expressed in Equation (6).

$$\sigma = \sigma' + [\aleph P_w + (1 - \aleph)P_a]I \tag{6}$$

In the equation, $\aleph$ is a function of the saturation S, and I represents the unit matrix. When the material is fully saturated, $\aleph = 1$; when the material is unsaturated, $\aleph = \aleph(S)$.

During the multi-stage hydraulic fracturing process, the pore pressure generated by the injection of the fracturing fluid into the formation significantly exceeds the original pore pressure of the formation. Based on this, the following assumptions are made: the desorption process of shale gas is neglected during multi-stage fracturing, and only the variation of pore pressure in the formation is analyzed, assuming that the formation is in a fully saturated state. Therefore, Equation (6) can be simplified as follows:

$$\sigma' = \sigma - P_w I \tag{7}$$

(2) Stress Equilibrium Equation

The stress equilibrium in the formation is represented using the principle of virtual work in the finite element method, and the equivalent stress at the fracture is expressed by Equation (10) [30].

$$\iiint_V (\sigma' + P_w I) : \delta\varepsilon dV = \iint_S T \cdot \delta v dS + \iiint_V f \cdot \delta v dV + \iiint_V sn\rho_w g \cdot \delta v dV \tag{8}$$

In the equation, δv represents the virtual displacement field; $\delta\varepsilon$ denotes the virtual strain, $\delta\varepsilon = sym(\partial\delta v/\partial x)$; T is the surface force per unit area; f represents the body force per unit volume (excluding fluid weight); n denotes the porosity; V represents the volume; S is the boundary area; ρ_w denotes the fluid density; and g represents the gravitational acceleration.

(3) Seepage Continuity Equation

The fluid within each element of the model is required to satisfy the continuity equation, meaning that the fluid inflow into the element must equal the rate of increase in fluid volume [31]. The mathematical expression is given in Equation (9).

$$\frac{d}{dt}\left(\iiint_V \frac{\rho_w}{\rho_w^0} sndV\right) = -\iint_S \frac{\rho_w}{\rho_w^0} sn\boldsymbol{n} \cdot v_w dS \tag{9}$$

In the equation, v_w represents the average velocity of fluid inflow from the boundary S; $\boldsymbol{n}$ denotes the outward normal vector of the boundary S; and ρ_w^0 represents the reference density of the fluid.

(4) Relationship Between Formation Permeability and Permeability Coefficient

In the simulation of fluid–solid coupling using the ABAQUS finite element software (ABAQUS2021 Dassault SIMULIA, Paris, France), the permeability of the material is represented by the permeability coefficient k [32], as expressed in Equation (10).

$$\overline{k} = \frac{k_s}{(1 + \beta\sqrt{v_w \cdot v_w})}k \tag{10}$$

In the equation, $\overline{k}$ represents the dimensionless permeability coefficient; k denotes the permeability of a fully saturated medium; β is the velocity coefficient, which depends on the porosity of the material; v_w represents the fluid velocity; and k_s is the relationship

between permeability and the saturation of the wetting liquid. When the saturation $s = 1$, $k_s = 1$. In this study, the formation is assumed to be in a fully saturated state.

3.3. Finite Element Numerical Model for Platform Well Fracturing

(1) Geometry Model Development

Based on the distribution characteristics and simplified processing results of microseismic event points around Well X-6 and its neighboring wells (Stages 6 to 10), a finite element model of the lower branch of the fractured well on Platform X was established. The finite element modeling approach offers significant advantages in analyzing complex geometries and static stress distributions, supported by mature commercial solvers. It has been extensively validated in the field of rock mechanics and enables the seamless integration of fluid–solid coupling models, making it suitable for a stress analysis in reservoirs.

The model dimensions are 1100 m (length) × 700 m (width) × 300 m (height) and include three horizontal wells, X-4, X-5, and X-6, each with a spacing of 300 m, as shown in Figure 7a. According to the actual wellbore structure, each well in the numerical model consists of three components: casing, cement sheath, and formation. Figure 7b illustrates a two-dimensional cross-section of the composite model. In the finite element analysis, the Von Mises yield criterion was employed to model the nonlinear elastoplastic behavior of the casing under complex stress conditions. The Von Mises yield criterion assumes that material yielding depends on equivalent stress, independent of the stress direction, making it effective in describing the yielding behavior of casing under combined axial, radial, and tangential stresses. Key parameters incorporated in the model include the elastic modulus, Poisson's ratio, and yield strength of the materials, adequately reflecting the mechanical response characteristics of casing under high pressure and complex loading conditions. Additionally, the effects of pore pressure and fluid–solid coupling were considered for the formation and cement sheath, modeled using the pore-elastic theory.

The elastic moduli of the casing and cement sheath were set to 210 GPa and 10 GPa, respectively, with Poisson's ratios of 0.3 and 0.17. The casing was assumed to be an ideal elastoplastic material with a yield strength of 758 MPa. Based on field geological data, the formation primarily consists of gray-black and black shale. Combining the well logging interpretation results of Platform X, the average geological parameters of the fracturing stages 6 to 10 were used as target parameters, including in situ stress, elastic modulus, and Poisson's ratio. The initial elastic modulus of the formation was 43.43 GPa, and the Poisson's ratio was 0.22. The principal stresses were as follows: maximum horizontal stress of 102.63 MPa; minimum horizontal stress of 89.48 MPa; and vertical stress of 95.95 MPa. Detailed parameters are provided in Table 1.

According to Saint-Venant's principle, the influence of changes in rock mechanical parameters in the far-field formation on casing stress can be considered negligible. Therefore, the numerical model accounts only for the variations in pressure and mechanical parameters in the near-wellbore formation, dividing the formation into two regions.

Fracturing zone: The fracturing zone near the wellbore, which corresponds to the distribution area of microseismic event points (as shown in Figure 7c,d). By varying the pore pressure and rock mechanics parameters in this zone, where the rock mechanics parameters are dynamically adjusted through the control of field variables, the damage evolution in the fracturing zone is simulated to assess the impact of the fracturing process on the casing.

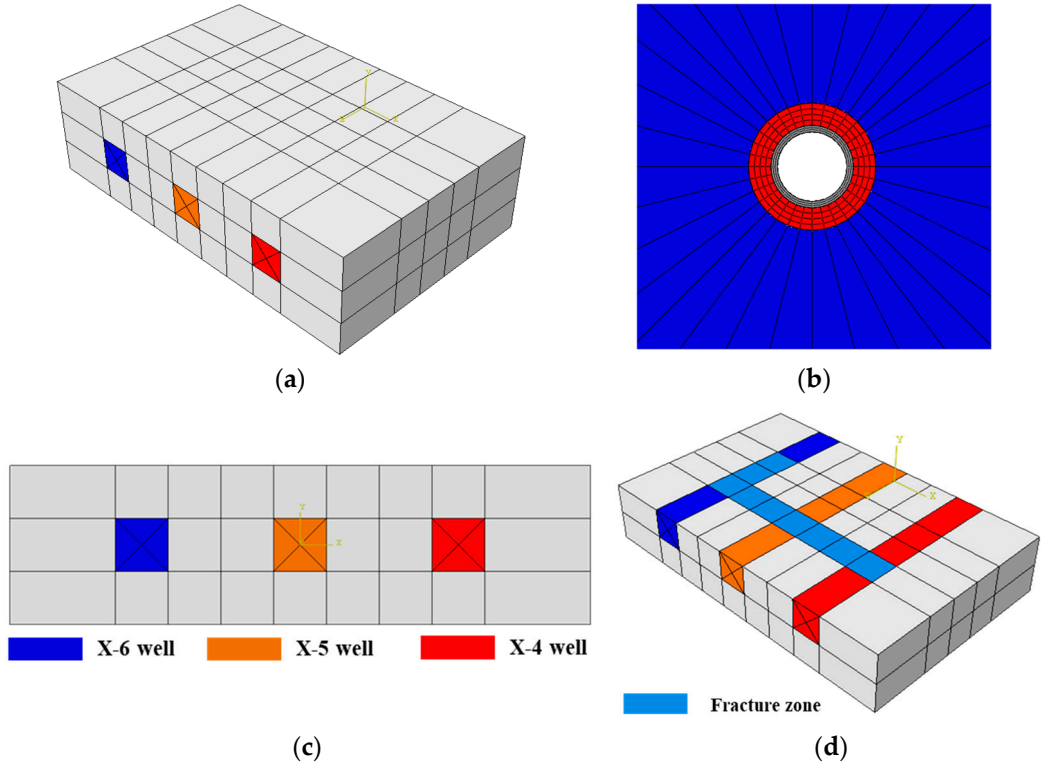

Figure 7. Finite element numerical modeling of platform well fracturing. (**a**) Finite element model. (**b**) Localized view of casing-cement formation assemblage. (**c**) Model cross-section. (**d**) Fracturing region.

Table 1. Geological parameters of fracturing stages in the X Platform formation.

Formation	Top Depth (m)	Bottom Depth (m)	Elastic Modulus (GPa)	Poisson's Ratio	Maximum Horizontal Principal Stress (MPa)	Minimum Horizontal Principal Stress (MPa)	Vertical Principal Stress (MPa)
$Longyi_1^3$	5009.5	5079.0	42.8	0.22	102.2	89.3	95.1
$Longyi_1^2$	5079.1	5132.9	43.6	0.22	103.3	89.2	95.5
$Longyi_1^1$	5132.9	5152.7	44.0	0.24	102.5	90.1	95.6
Wufeng	5152.7	5272.0	42.9	0.22	102.4	89	96.3
$Longyi_1^1$	5272.1	5306.7	43.5	0.22	102.3	89.5	96.8
$Longyi_1^2$	5306.7	5372.0	43.8	0.22	103.1	89.8	96.4
Average Value	-	-	43.43	0.22	102.63	89.48	95.95

Unfractured zone: The area far from the wellbore, where the rock mechanical parameters remain unchanged during calculations. This region represents the unfractured formation beyond the fracture network.

This partitioning approach enables a more precise representation of the impact of fracturing on casing stress near the wellbore while simplifying the computational complexity of the far-field formation.

(2) Mesh Generation

For the mesh generation, structured grids with uniform divisions were applied to both the casing and the cement sheath. Since the casing does not involve pore permeability characteristics, it was meshed using three-dimensional eight-node hexahedral elements with reduced integration (C3D8R). For the cement sheath, which is involved in the fluid–

solid coupling processes, C3D8P elements with pore pressure coupling were used. For the complex formation body (including both unfractured and fractured regions), the formation was first divided into multiple regions to facilitate automatic meshing. The overall seed density of the model was controlled, with local refinement applied to the casing region. Finally, free sweep meshing techniques were used to complete the meshing process. As the porous rock formation is similar to the cement sheath in involving fluid–solid coupling processes, the same three-dimensional eight-node hexahedral C3D8P elements were selected for the formation.

(3) Boundary Conditions and Load Settings

Two types of analysis steps were set in the model:

Geostatic Analysis Step, which was used to simulate the equilibrium of formation skeleton stress and pore pressure prior to fracturing.

Soil Coupling Analysis Steps, where multiple soil coupling analysis steps were used to simulate the dynamic changes during multi-stage fracturing.

For boundary conditions, full displacement constraints were applied to the six far-field boundary surfaces of the model, and the pore pressure boundary was set to equal the initial formation pressure to ensure that the boundary conditions align with the actual operating conditions. For load settings, the casing internal pressure was adjusted to simulate the multi-stage fracturing process. During fluid injection, the casing internal pressure was set as the sum of the pump pressure and the hydrostatic column pressure. During the non-injection phases, the casing internal pressure was set as the sum of the wellhead back pressure and the hydrostatic column pressure. Additionally, the initial stress field conditions were applied using the Predefined Field feature, with specific geo-stress values detailed in Table 1.

(4) Model Assumptions and Limitations

The following assumptions were made in this study: the rock material is homogeneous and isotropic, and the processes of fracture propagation and pore pressure diffusion are quasi-static. These assumptions simplify the complex geological conditions and dynamic effects, making the model computationally more efficient. However, they may overlook the influence of regional geological heterogeneity and the dynamic effects on stress distribution. Additionally, the boundary conditions were set as a static uniform distribution of far-field stresses, which might not fully capture the effects of stress interactions with neighboring wells or local natural fracture connectivity on the stress field.

4. Results and Discussion

Based on the multi-stage hydraulic fracturing finite element model developed for platform wells, numerical simulations were performed for Stages 6–10 of Well X-6. The simulations yielded results for formation pressure, casing stress, and displacement for each fracturing stage on Platform X. This study focuses on analyzing the changes in formation stress, casing stress, and displacement around the unfractured Wells X-4 and X-5 under the influence of fracturing operations in neighboring wells.

4.1. Variation Characteristics of Pore Pressure and Geo-Stress Around Unfractured Wells on the Platform

Considering that the horizontal wellbore is oriented perpendicular to the direction of the maximum horizontal principal stress, the variations in stress in this direction have a more significant impact on the wellbore. The horizontal sections of Wells X-4 and X-5 were selected for the analysis, and the pore pressure and geo-stress values at different fracturing stages were extracted to examine the variation characteristics of pore pressure

and maximum horizontal principal stress around the unfractured wells during the multi-stage fracturing.

(1) Pore Pressure Variation

Figure 8a,b illustrate the variation characteristics of pore pressure around Wells X-4 and X-5 during different fracturing stages. As shown, during Stages 6 to 8 of the fracturing in Well X-6, the impact on pore pressure around the unfractured wells was minimal, with an increase of only 3–7 MPa. However, during Stage 9, the hydraulic fractures connected with natural fracture zones, causing significant increases in pore pressure around both Wells X-4 and X-5. Due to the differing distances between the two wells, the magnitude of the pore pressure increase also varied, with increases of 27.08 MPa and 45.58 MPa compared to the initial pore pressure, respectively. Further expansion of the natural fractures during Stage 10 resulted in additional connectivity between the hydraulic and natural fractures, leading to continuous increases in pore pressure around the wells. The increases reached 35.61 MPa and 58.89 MPa for Wells X-4 and X-5, respectively. These results indicate that the presence of natural fractures significantly amplifies the changes in pore pressure around the unfractured wells.

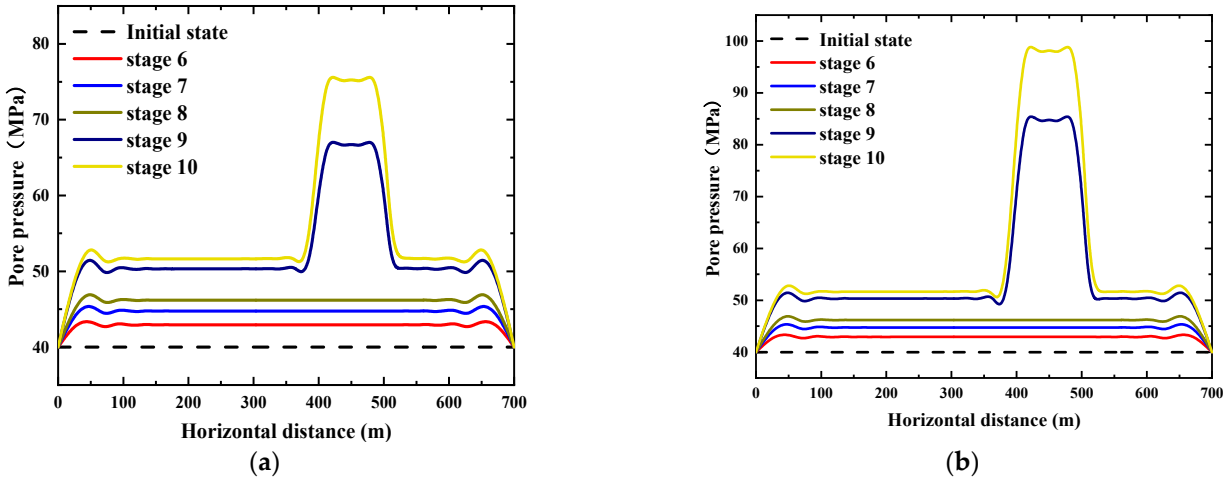

Figure 8. Characterization of pore pressure variations around unfractured wells. (**a**) Well X-4. (**b**) Well X-5.

(2) Maximum Horizontal Principal Stress

Figure 9a,b illustrate the variation characteristics of the maximum horizontal principal stress around Wells X-4 and X-5 during different fracturing stages. As shown, the variation trend of the maximum horizontal principal stress closely resembles the characteristics of pore pressure changes. During Stage 9 fracturing, the maximum horizontal principal stress around Wells X-4 and X-5 increased significantly, with increments of 22.83 MPa and 36.98 MPa compared to the initial maximum horizontal principal stress, corresponding to increases of 20.83% and 33.74%, respectively. As Stage 10, the fracturing progressed, and further connectivity between the hydraulic fractures and natural fractures led to continued increases in the maximum horizontal principal stress, with increments reaching 28.95 MPa and 46.56 MPa, corresponding to increases of 26.41% and 41.57%, respectively. These results indicate that as the hydraulic fractures further connect with the natural fractures, the maximum horizontal principal stress around the unfractured wells increases significantly. Moreover, Well X-5 experiences a notably greater impact compared to Well X-4.

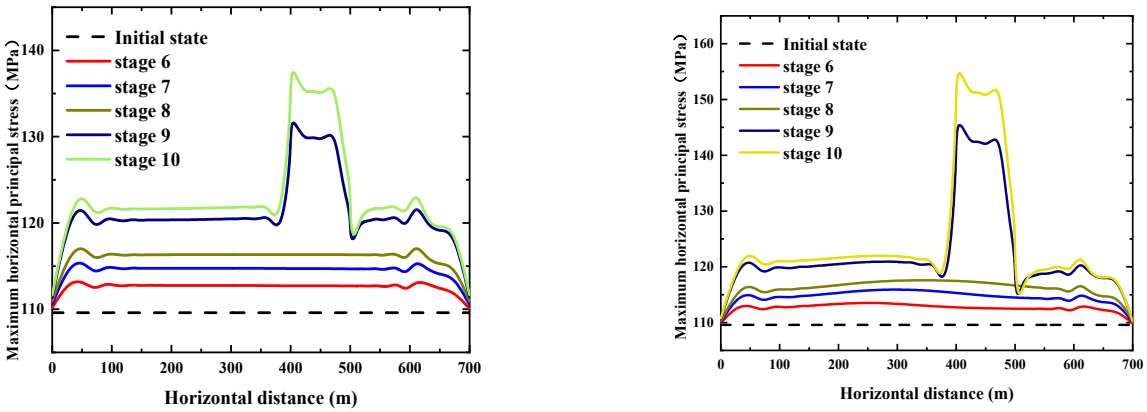

Figure 9. Characterization of maximum horizontal principal stress variations around unfractured wells. (**a**) Well X-4. (**b**) Well X-5.

4.2. Variation Characteristics of Casing Stress in Platform Wells

Multi-stage fracturing operations induce changes in geo-stress around the wellbore, resulting in a more complex loading environment for the wellbore casing. The loads experienced by the casing become increasingly diversified. In this section, the Von Mises equivalent stress (hereafter referred to as Mises stress) is employed to describe the stress state of the casing in the fractured well and adjacent unfractured wells. Mises stress provides a comprehensive representation of the stress distribution characteristics of the casing under multi-stage fracturing. Combined with the material yield criterion, it is used to determine whether the casing reaches its yield strength under complex loads, thus enabling an evaluation of the mechanical performance and safety of the casing.

(1) Fractured Well

Figure 10 presents the Mises stress distribution contour of the casing in Well X-6 before and after fracturing, as well as the variation characteristics of casing stress across different fracturing stages. As shown in Figure 10a, prior to fracturing, the maximum stress on the casing under the initial geo-stress was 562.6 MPa. After fracturing in Stages 6 to 10, the maximum stress increased to 724.4 MPa, remaining below the yield strength of the casing material (Figure 10b). A further analysis of the casing stress variation with the fracturing stages (Figure 10c) reveals that during Stages 6 to 8, the increase in casing stress was relatively small, approximately 7 MPa. However, during Stages 9 to 10, the hydraulic fractures connected with natural fractures, resulting in a significant increase in casing stress. Specifically, the stress increment after Stage 9 fracturing was 15.94 MPa, while the increment after Stage 10 fracturing further increased to 20.64 MPa.

(2) Unfractured Well

Figure 11 illustrates the variation in the maximum Mises stress of the casing in Well X-4 during different fracturing stages. As shown, during Stages 6 to 8, the casing stress in Well X-4 gradually increased under the influence of fracturing operations in the adjacent well. Due to the relatively large distance between the two wells, the stress increment in the casing was comparatively small. By the end of Stage 8, the casing stress had increased by 26.2 MPa compared to its initial state. When the fracturing progressed to Stages 9 and 10, the hydraulic fractures connected with the natural fracture zone, allowing for high-pressure fracturing fluid to diffuse along the natural fractures. This caused localized stress concentration in Well X-4, leading to a significant increase in the casing stress. The maximum casing stress reached 667.3 MPa, although it remained below the yield strength of the casing material.

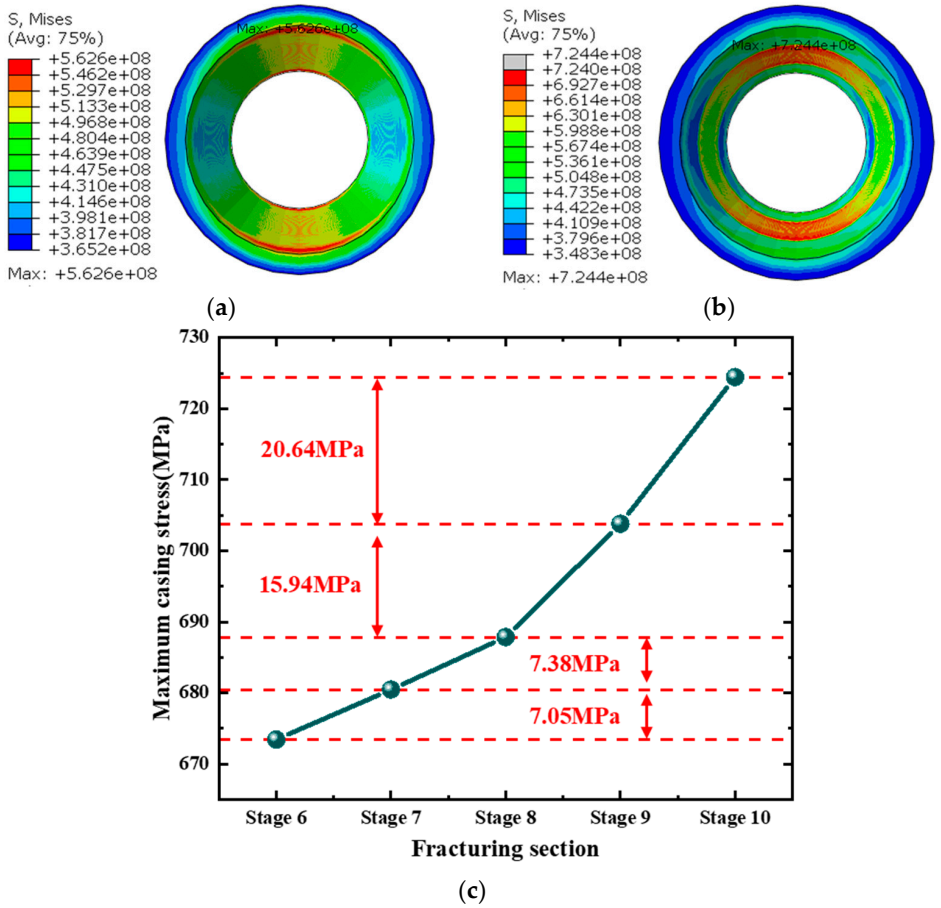

Figure 10. Characterization of casing stress changes in Well X-6. (**a**) Before fracturing. (**b**) After fracturing. (**c**) Casing stress changes at different fracturing stages.

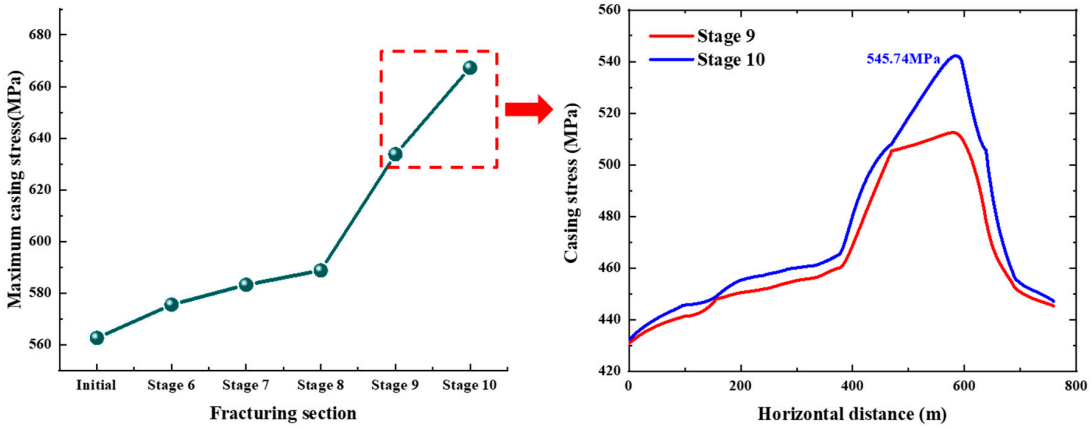

Figure 11. Characteristics of casing stress changes in Well X-4 at different fracturing stages.

Figure 12 illustrates the variation in casing stress in Well X-5 after each fracturing stage and presents the stress contour plot of the casing following the completion of fracturing. The stress variation trend in the casing of Well X-5 is similar to that of Well X-4. However, due to the closer proximity of Well X-5 to the fractured well, the impact of fracturing operations is more pronounced. After the Stage 8 fracturing, the casing stress in Well X-5 increased by 41.1 MPa, which is 14.9 MPa higher than the increment observed in Well X-4. During Stages 9 and 10, the localized stress concentration further increased the casing stress significantly, with the maximum stress reaching 796.54 MPa, exceeding its

yield strength of 758 MPa. Additionally, the computed stress contour plot indicates that noticeable deformation occurred at the location where the fractures were connected.

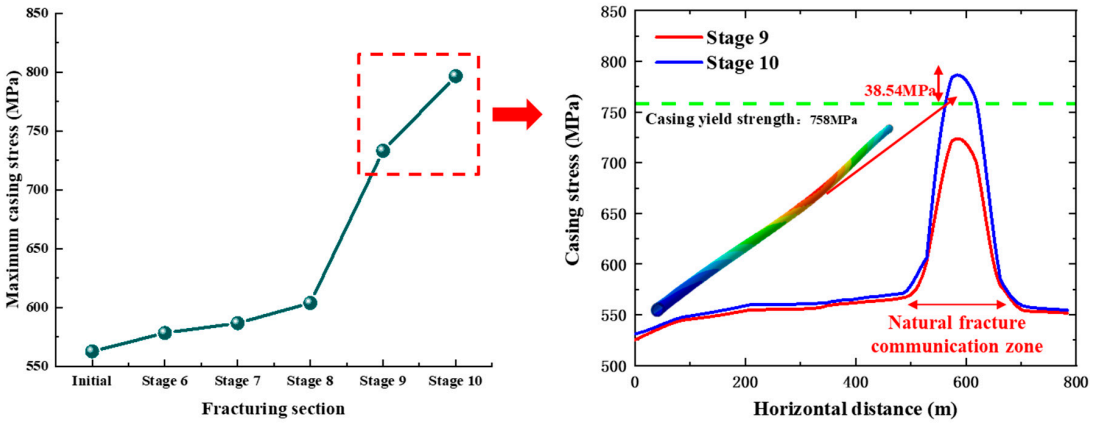

Figure 12. Characteristics of casing stress change in Well X-5 at different fracturing stages.

A further analysis was conducted on the circumferential stress distribution of the casing at two points in Well X-5, one at the connected fracture location and the other at the unconnected fracture location, to investigate the impact of adjacent well fracturing operations on the circumferential stress of the casing at different positions (as shown in Figure 13). Overall, the circumferential stress at both points exhibited a sinusoidal periodic variation pattern, with the maximum stress occurring in the direction of the maximum horizontal principal stress (i.e., at circumferential angles of 90° and 270°). However, significant differences were observed in the stress values between the two points. At the unconnected fracture location, the maximum circumferential stress of the casing was 562.60 MPa. Due to the difference in the original in situ stresses (maximum horizontal principal stress and vertical principal stress), a circumferential stress difference was generated, with a maximum difference of 107.99 MPa. In contrast, at the connected fracture location, the circumferential stress of the casing increased significantly. The circumferential stress in the direction of the maximum horizontal principal stress reached 796.49 MPa, exceeding the yield strength by 38.49 MPa. This indicates that the casing is more prone to compressive deformation in the direction of the horizontal principal stress, resulting in a reduced casing inner diameter, which could lead to issues such as bridge plug obstruction.

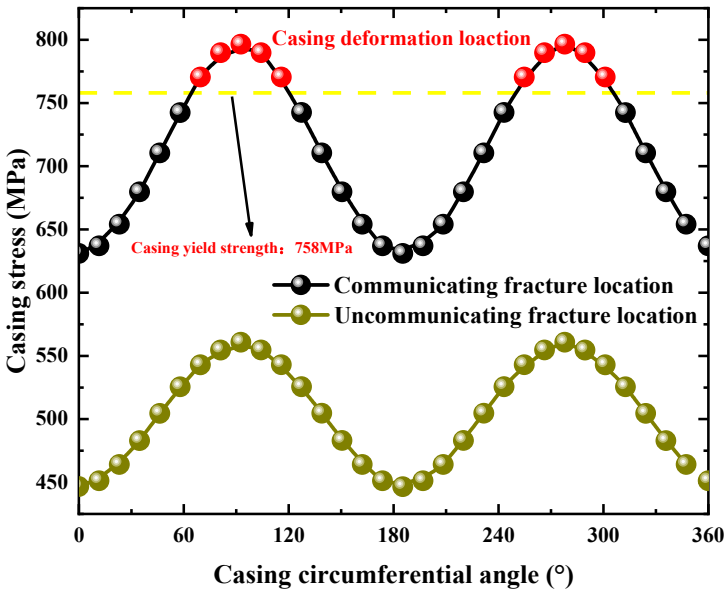

Figure 13. Characteristics of casing circumferential stress distribution at different locations in Well X-5.

4.3. Displacement Variation Characteristics of the Casing in Well X-5

To more intuitively investigate the casing deformation, the displacement in the direction of the maximum principal stress was extracted along the entire casing section of Well X-5, and the displacement variation characteristics of the casing at different fracturing stages were analyzed.

Figure 14 presents the displacement in the direction of the maximum principal stress for the casing in Well X-5 during different fracturing stages. As shown, prior to the fracturing operations, the casing experienced negligible deformation under the compressive action of the initial in situ stress field, with the maximum displacement in the direction of the maximum principal stress being only 0.22 mm. This indicates that the casing was in an intact state under the initial stress field, without significant deformation or failure issues. However, following the platform well staged fracturing operations, the hydraulic fractures connected with the fracture zones, allowing for the fracturing fluid to diffuse along the direction of the fracture development to the vicinity of the unfractured well. This caused concentrated loading on the wellbore, leading to noticeable deformation of the casing in the fracture-connected region of the unfractured well. The maximum displacement in the direction of the maximum principal stress reached 13.21 mm, with a deformation rate of 11.14%.

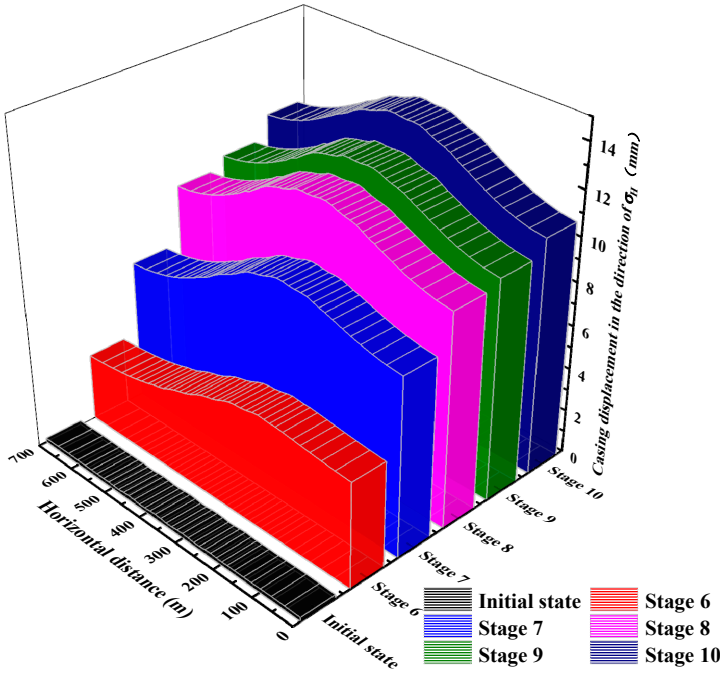

Figure 14. Deformation displacement of Well X-5 casing in the direction of the maximum principal stress at different fracturing stages.

Field data from Well X-5 revealed that a bridge plug encountered obstruction at a depth of 4593 m. Multi-arm caliper logging indicated casing deformation in the range of 4591.7 m to 4593.28 m (Figure 15), with a maximum deformation of 14.94 mm and a deformation rate of 12.59%. A comparison of the finite element numerical simulation results with the field observations revealed consistency, with an error of only 1.45%. This demonstrates that the numerical simulation accurately reflects the actual casing deformation observed in the field, providing a reliable basis for subsequent research.

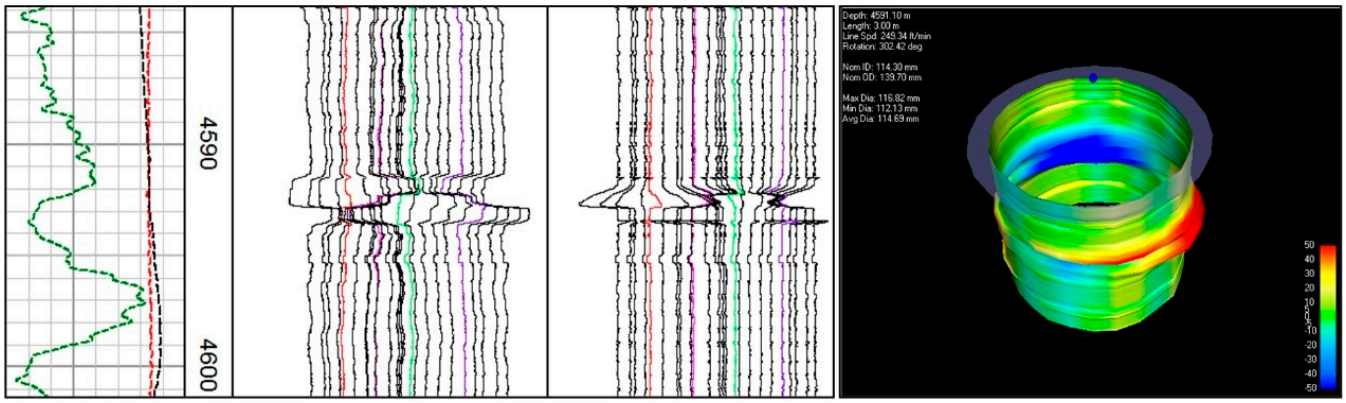

Figure 15. Interpreted results of multi-arm well log measurement at 4591.7–4593.28 m in Well X-5.

5. Measure to Prevent Casing Deformation

The phenomenon of "pre-deformation without fracturing" in platform wells significantly impacts the fracturing efficiency and single-well production. Effectively preventing and mitigating casing deformation in unfractured shale gas platform wells remains a critical challenge in the development of shale gas wells in the Luzhou block. Based on the multi-stage hydraulic fracturing numerical model developed earlier and a thorough analysis of the deformation mechanism of unfractured well casings on the same platform, this study proposes a method to prevent casing deformation in unfractured platform wells: pre-pressurization of the casing.

5.1. Control Mechanism of Pre-Deformation Prevention in Platform Wells

Pre-pressurization of the casing refers to injecting a predetermined internal pressure into the casing of adjacent unfractured wells prior to fracturing operations in platform wells. This pre-pressurization acts as a countermeasure against the concentrated loading caused by the connectivity of the natural fractures during fracturing in adjacent wells, thereby preventing casing deformation in unfractured wells under stress concentration, as illustrated in Figure 16. By employing the pre-pressurization method, the impact of localized stress concentrations on the casing can be effectively reduced, thereby enhancing the structural integrity of the casing in unfractured wells and ensuring the overall effectiveness of the fracturing operations.

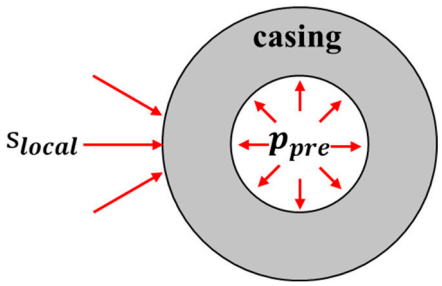

Figure 16. Prevention and control schematic.

Based on the multi-stage hydraulic fracturing finite element numerical model established in Section 2.3, the effects of pre-pressurization in the casing of an unfractured well were simulated during the fracturing process of Well X-6 by applying varying levels of internal pressure to the inner wall of the casing in Well X-5. In this section, the internal pressure in the casing of Well X-5 was set to 20 MPa, and the stress variation characteristics of the unfractured well casing (i.e., Well X-5) during the fracturing process of Well X-6 were analyzed. The results are shown in Figure 17.

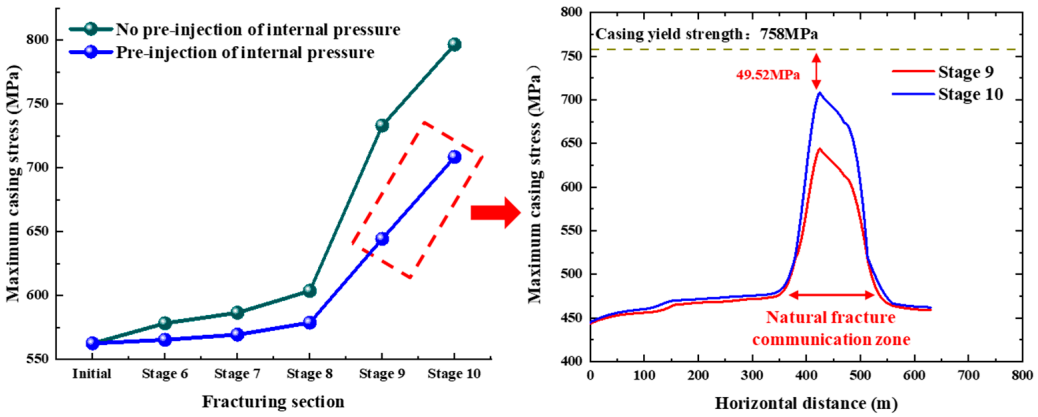

Figure 17. Characterization of casing stress changes in unfractured wells under pre-injection of internal pressure of 20 MPa.

As observed in Figure 17, compared to the condition without internal pressure, applying a pre-injection pressure of 20 MPa resulted in an overall reduction in the casing stress for the unfractured well. After the Stage 8 fracturing, the stress increment in the casing was 15.83 MPa, which was 25.27 MPa lower than the increment under the condition without internal pressure. When the hydraulic fractures connected with the natural fractures, the casing stress in the unfractured well also increased significantly; however, the maximum stress only reached 708.48 MPa, remaining below the yield strength of the casing (758 MPa). Compared to the maximum Mises stress of 796.50 MPa under conditions without pre-pressurization, the maximum stress in the casing was reduced by 88.02 MPa, which is a decrease of 11.05%, with pre-pressurization. This result effectively reduced the risk of casing deformation in the unfractured well, demonstrating the feasibility and effectiveness of the pre-pressurization method.

5.2. Effect of Different Pre-Injection Internal Pressures on Casing Stress

To further analyze the impact of different pre-injection internal pressure values on the casing stress of unfractured wells and provide guidance for field operations, the internal pressure in Well X-5 was set to 5 MPa, 10 MPa, 15 MPa, and 20 MPa, respectively. The variation in the maximum stress of the casing in Well X-5 during fracturing was investigated and compared to the casing stress under conditions without pre-injection pressure, as shown in Figure 18.

As illustrated in Figure 18, the maximum stress in the casing of Well X-5 decreased progressively across all fracturing stages as the pre-injection internal pressure increased. After the Stage 10 fracturing, compared to the condition without pre-injection pressure, the maximum casing stress was reduced by 27.31 MPa, 49.42 MPa, 71.50 MPa, and 88.02 MPa for pre-injection pressures of 5 MPa, 10 MPa, and 20 MPa, respectively. When the pre-injection pressure reached 10 MPa, the maximum Mises stress in the casing of the unfractured well decreased to 747.08 MPa, which is below the casing's yield strength, effectively reducing the risk of casing deformation.

By applying a predetermined level of casing internal pressure to the unfractured wells in advance, the phenomenon of pre-deformation caused by the fracturing of adjacent wells can be significantly mitigated. Based on simulation results, a pre-injection pressure of 10 MPa can be considered a reference value for field applications.

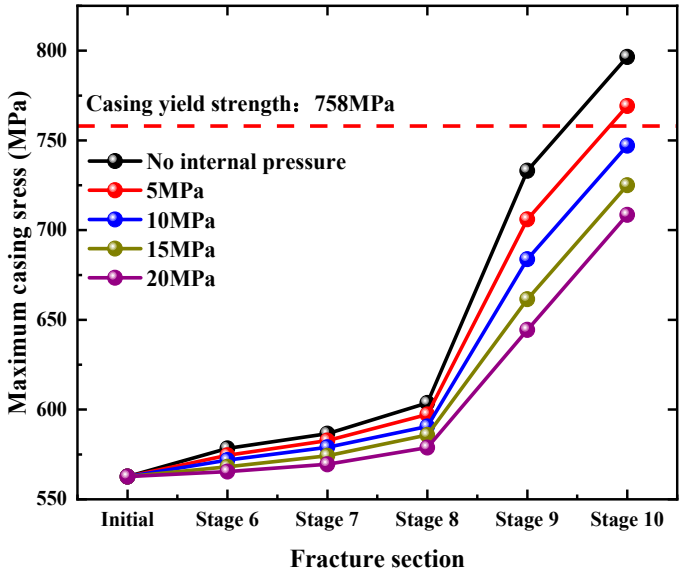

Figure 18. Characteristics of casing stress changes in unfractured wells under different internal pressure conditions.

6. Conclusions

(1) A high casing deformation rate has been observed in the Luzhou block, with prominent "pre-deformation" phenomena in the platform wells and severe casing deformation. The locations of the casing deformation points are found to be highly correlated with faults and natural fractures. The development of fracture systems is considered a major factor contributing to the large number of wells experiencing pre-deformation.

(2) Multi-stage fracturing operations in platform wells significantly increase the pore pressure and in situ stress around adjacent unfractured wells. This effect becomes particularly pronounced when hydraulic fractures intersect with the fracture system, allowing high-pressure fracturing fluid to propagate along the fracture trajectory toward neighboring wells, thereby causing a significant increase in stress around unfractured wells.

(3) The increase in in situ stress around unfractured wells imposes localized high loads on the wellbore, significantly elevating the casing stress. This ultimately results in casing deformation and the occurrence of "pre-deformation" phenomena.

(4) Prior to fracturing operations in platform wells, the injection of a predetermined level of internal pressure into the casing of adjacent unfractured wells has been shown to effectively reduce the casing stress caused by stress concentration, thereby mitigating the risk of casing deformation.

7. Future Work

To address the limitations of the current model, future research could be conducted by incorporating the anisotropic and heterogeneous properties of rock to more accurately represent the complex geological conditions. The optimization of boundary condition settings is recommended, and the influence of neighboring well stress fields and fracture connectivity should be included to expand the applicability of the model and the findings presented in this study.

Author Contributions: Writing—original draft, X.Z. and Y.Z.; funding acquisition, J.L.; formal analysis, X.Z.; data curation, W.C. and Z.L.; validation, W.Z. and G.L.; methodology, X.Z. All authors have read and agreed to the published version of the manuscript.

Funding: The paper was supported by the National Natural Science Foundation of China "Life cycle seal integrity theory and control method on cement sheath in complex environment (NO. U22B6003)", "Basic research on prevention and control of sustained casing pressure in deep and ultra-deep gas wells in Sichuan basin (NO. U22A20164)", the Basic Research on Prevention and Control of Sustained Casing Pressure in Deep and Ultra-Deep Gas Wells in Sichuan Basin (NO. U23B2081), and the Strategic Cooperation Technology Projects of CNPC and CUPB (NO. ZLZX2020-01).

Data Availability Statement: The original contributions presented in this study are included in the article. Further inquiries can be directed to the corresponding author.

Conflicts of Interest: Authors Yuxuan Zhao, Wenbo Zhang, and Zongyu Lu were employed by the company Xinjiang Oilfield Company. Author Wei Cao was employed by the company Sichuan Jewel Flower Xinsheng Oil & Gas Operation Service Co. The remaining authors declare that the research was conducted in the absence of any commercial or financial relationships that could be construed as a potential conflict of interest. The Xinjiang Oilfield Company and Sichuan Jewel Flower Xinsheng Oil & Gas Operation Service Co. had no role in the design of the study; in the collection, analyses, or interpretation of data; in the writing of the manuscript, or in the decision to publish the results.

References

1. Ma, X.; Xie, J.; Yong, R.; Zhu, Y. Geological characteristics and high production control factors of shale gas reservoirs in Silurian Longmaxi Formation, southern Sichuan Basin, SW China. *Pet. Explor. Dev.* **2020**, *47*, 901–915. [CrossRef]
2. Han, L.; Li, X.; Liu, Z.; Guo, W.; Cui, Y.; Qian, C.; Huang, Y. Study on rock mechanics characteristics of deep shale in Luzhou block and the influence on reservoir fracturing. *Energy Sci. Eng.* **2023**, *11*, 4–21. [CrossRef]
3. Liu, Z.; Pan, Z.; Li, S.; Zhang, L.; Wang, F.; Han, L.; Zhang, J.; Ma, Y.; Li, W.; Li, W. Study on the effect of cemented natural fractures on hydraulic fracture propagation in volcanic reservoirs. *Energy* **2022**, *241*, 122845. [CrossRef]
4. Jin, Y.; Zhao, Q.; Mou, Y.; Wei, Y.; Cui, Y.; Hu, Y.; Wang, M.; Dong, T. Discussion on formation mechanism of casing deformation in horizontal wells in deep shale gas of Luzhou area. *Nat. Gas Ind.* **2024**, *44*, 99–110.
5. Han, L.; Li, X.; Liu, Z.; Duan, G.; Wan, Y.; Guo, X.; Guo, W.; Cui, Y. Influencing factors and prevention measures of casing deformation in deep shale gas wells in Luzhou block, southern Sichuan Basin, SW China. *Pet. Explor. Dev.* **2023**, *50*, 979–988. [CrossRef]
6. Lu, Z.; Lian, W.; Li, J.; Wang, N. Analysis of influencing factors of slippage and the dynamic process of fault slip caused by multi-stage fracturing. *Processes* **2024**, *12*, 448. [CrossRef]
7. Chiaramonte, L.; Zoback, M.D.; Friedmann, J.; Stamp, V. Seal integrity and feasibility of CO2 sequestration in the Teapot Dome EOR pilot: Geomechanical site characterization. *Environ. Geol.* **2008**, *54*, 1667–1675. [CrossRef]
8. Chipperfield, S.T.; Wong, J.R.; Warner, D.S.; Cipolla, C.L.; Mayerhofer, M.J.; Lolon, E.P.; Warpinski, N.R. Shear dilation diagnostics—A new approach for evaluating tight gas stimulation treatments. *APPEA J.* **2007**, *47*, 221–238. [CrossRef]
9. Dong, K.; Liu, N.; Chen, Z.; Huang, R.; Ding, J.; Niu, G. Geomechanical analysis on casing deformation in Longmaxi shale formation. *J. Pet. Sci. Eng.* **2019**, *177*, 724–733. [CrossRef]
10. Huang, R.; Chen, Z.; Zeng, B.; Song, Y.; Zhou, X. Casing Deformation Caused by Hydraulic Fracturing-Induced Fault Slip in Sichuan Basin and Optimization of Treatment Parameters. In *IOP Conference Series: Earth and Environmental Science*; IOP Publishing: Bristol, UK, 2020; Volume 570, p. 022057.
11. Chen, C.; Cao, H.; Zhou, X.; Gou, Q.; Zhang, H. Correlation Between Casing Deformation and Fracture zonesin Changning Shale Gas block, Sichuan Basin. *Nat. Gas Explor. Dev.* **2020**, *43*, 123–130.
12. Yin, F.; Han, L.; Yang, S.; Deng, Y.; He, Y.; Wu, X. Casing deformation from fracture slip in hydraulic fracturing. *J. Pet. Sci. Eng.* **2018**, *166*, 235–241. [CrossRef]
13. Yin, F.; Xiao, Y.; Han, L.; Wu, X. Quantifying the induced fracture slip and casing deformation in hydraulically fracturing shale gas wells. *J. Nat. Gas Sci. Eng.* **2018**, *60*, 103–111. [CrossRef]
14. Xu, Z.; Wu, X.; Yin, F.; Han, L.; Yang, S. Mechanism study of casing deformation in multistage hydraulic fracturing shale reservoir. In Proceedings of the Unconventional Resources Technology Conference, Houston, TX, USA, 23–25 July 2018; Society of Exploration Geophysicists: Houston, TX, USA; American Association of Petroleum Geologists: Tulsa, OK, USA; Society of Petroleum Engineers: Richardson, TX, USA, 2018; pp. 144–151.
15. Zhao, C.; Li, J.; Liu, G.; Zhang, X. Analysis of well stress with the effect of natural fracture nearby wellbore during hydraulic fracturing in shale gas wells. *J. Pet. Sci. Eng.* **2020**, *188*, 106885. [CrossRef]
16. Zhao, C.; Jin, Y.; Wang, X. Investigation on dynamic mechanism of fault slip and casing deformation during multi-fracturing in shale gas wells. *Sci. Rep.* **2024**, *14*, 13164. [CrossRef] [PubMed]

17. Liu, P.; Li, J.; Yang, H.; Zhang, H.; Lian, W.; Gao, R.; Zhang, X. Study on a new method of controlling casing shear deformation based on hollow glass microspheres cement sheath. *Energy Rep.* **2022**, *8*, 5192–5203. [CrossRef]
18. Zhao, C. Investigation on Failure Mechanism and Test of Casing Deformation in Shale Gas Wells During Multi-Fracturing. Ph.D. Dissertation, China University of Petroleum, Beijing, China, 2021.
19. Tong, H.; Liu, Z.; Zhang, H.; Zhang, P.; Deng, C.; Ren, X.; Xiao, K.; Zhou, Y. Theory and Method of Temporary Macrofracture Plugging to Prevent Casing Deformation in Shale gas Horizontal Wells. *Nat. Gas Ind.* **2021**, *41*, 92–100.
20. Tong, H.; Zhang, P.; Zhang, H.; Liu, Z.; Ren, X.; Xiao, K.; Zhou, Y.; Deng, C. Geomechanical Mechanisms and Prevention Countermeasures of Casing Deformation in Shale gas Horizontal Wells. *Nat. Gas Ind.* **2021**, *41*, 189–197.
21. Chen, C.; Huang, R.; Zeng, B.; Song, Y.; Zhou, X. Analysis and Optimization of Construction Parameters for Preventing Casing Deformation in the Changning Shale Gas Block, Sichuan Basin. *Pet. Drill. Tech.* **2021**, *49*, 93–100.
22. Lu, Q.; Liu, Z.; Guo, J.; He, L.; Li, Y.; Zeng, J.; Ren, S. Hydraulic fracturing induced casing shear deformation and a prediction model of casing deformation. *Pet. Explor. Dev.* **2021**, *48*, 460–468. [CrossRef]
23. Lei, Q.; Chen, C.; Liu, S.; Zhu, X. A study on governance method of casing shear deformation in shale gas well. *J. Mech. Sci. Technol.* **2024**, *38*, 639–648. [CrossRef]
24. Lei, Q.; Zhang, J.; Zhu, X.; Shi, C.; Chen, C.; He, W. Experimental study on shear deformation mechanism and mitigation in shale gas casing. *Eng. Fail. Anal.* **2024**, *159*, 108056. [CrossRef]
25. Biot, M.A. Mechanics of deformation and acoustic propagation in porous media. *J. Appl. Phys.* **1962**, *33*, 1482–1498. [CrossRef]
26. Biot, M.A. Theory of elasticity and consolidation for a porous anisotropic solid. *J. Appl. Phys.* **1955**, *26*, 182–185. [CrossRef]
27. Liang, T.; Jin, F. Analysis on concrete dams based on the concept of generalized effective stress. *J. Hydroelectr. Eng.* **2009**, *28*, 47–51.
28. Lu, C.; Li, Z.; Li, D. Problems of applying seepage pressure in coupling analysis of seepage and stress using ABAQUS. *J. Yangtze River Sci. Res. Inst.* **2018**, *35*, 68.
29. Zhang, W. *Seepage and Stress Coupling Model for Shale Reservoir and Its Application*; China University of Mining and Technology: Beijing, China, 2015.
30. Chang, X.; Yuan, X. Application of strength reduction method considering hydro-mechanical coupling to analyze anti-sliding stability of gravity dams. *Eng. J. Wuhan Univ./Wuhan Daxue Xuebao* **2012**, *45*, 545–549.
31. Yang, T.; Tang, C.; Liang, Z.; Li, L.; Zhu, W.; Tan, G. Numerical Modeling Study on Damage and Seepage Coupling During the Fracture Process of Brittle Rocks. *Chin. J. Theor. Appl. Mech.* **2003**, *35*, 533–541.
32. Chai, J.; Wu, Y. Mathematical model for couple analysis of seepage and stress fields in RCCD. *J. Hydraul. Eng.* **2000**, *9*, 33–36.

Disclaimer/Publisher's Note: The statements, opinions and data contained in all publications are solely those of the individual author(s) and contributor(s) and not of MDPI and/or the editor(s). MDPI and/or the editor(s) disclaim responsibility for any injury to people or property resulting from any ideas, methods, instructions or products referred to in the content.